Chondrogenic Cancer Grading by combining Machine and Deep Learning with Raman Spectra of Histopathological Tissues

Gianmarco Lazzini and Mario D'Acunto *

Posted Date: 29 January 2024

doi: 10.20944/preprints202401.1935.v1

Keywords: Chondrosarcoma; Enchondroma; Confocal Raman Microscopy; Machine Learning, Deep Learning; Permutation Feature Importance

Article

Chondrogenic Cancer Grading by combining Machine and Deep Learning with Raman Spectra of Histopathological Tissues

Gianmarco Lazzini and Mario D'Acunto *

[1] CNR-IBF Consiglio Nazionale delle Ricerche, Istituto di Biofisica; via Moruzzi 1, I-56124, Pisa, Italy
gianmarco.lazzini@ibf.cnr.it
* Correspondence: mario.dacunto@ibf.cnr.it

Abstract: The present paper explored the possibility of discriminating between different malignant degrees of Chondrosarcoma (CS), a diffused bone tumor, and Enchondroma (EC), its benign version, through an approach based on the coupling between Confocal Raman Microscopy (CRM) and Machine Learning (ML) techniques. Recently, Raman Spectroscopy has proven to be a powerful tool for a complete grading of CS by distinguishing between grade 1, 2 and 3, and to distinguish CS from EC. In this paper, we tested some models, belonging either to ML or to the sub-type called Deep Learning (DL), showing excellent classification performances, especially the DL algorithms, with classification accuracy approaching to 100%, making the models promising for future implementations of Raman spectroscopy when applied to oncology diagnosis. In turn, we highlighted how some proper ML models result in worse classification performances but better resolution of specific chemical target compounds, possible candidate to become malignant markers, with relevant implication for a correct diagnosis.

Keywords: Chondrosarcoma; Enchondroma; Confocal Raman Microscopy; Machine Learning, Deep Learning; Permutation Feature Importance

1. Introduction

Chondrosarcoma (CS) turns out to be the second most common form of primary bone tumor worldwide, with almost seven cases per million people registered every year [1]. In the continuous effort to introduce effective and minimally invasive therapies, the ability in grading CS and in distinguishing this form of bone cancer from healthy tissues and/or benign tumors, such as Enchondroma (EC), represents a crucial factor. The common protocol for the diagnosis of CS is based on an initial examination of radiological and/or Magnetic Resonance (MRI) images, followed by the histopathological analysis of a tissue biopsy. One of the drawbacks of this procedure is represented by the frequent discrepancies between the response of pre- and post-surgical histopathological analysis, mainly due to the presence of tissue inhomogeneities within the same tumor mass. This last feature also determines the presence of not-well defined tumor margins, undoubtedly affecting the outcome of the surgical therapies. In particular, setups for image-guided surgery, Computed Tomography (CT) and MRI have been introduced to help the surgeon in maximizing the size of the excised tumor mass by preserving the surrounding healthy tissues. Despite the progress of these techniques, they still show weaknesses. In particular, CT is based on the use of ionizing radiation, with possible side-effects for the patient and/or the operator. Furthermore, MRI employs intense magnetic fields, not suitable for patients with metallic devices implanted within the body.

Traditionally, biopsy is the standard methodology for the pathological diagnosis of cancerous tissues. However, this technique typically involves tissue sectioning and staining, basically requiring pathologists with specialized training in order to interpret correctly tissues samples. On the contrary, despite its intrinsically low acquisition speed, the Raman Spectroscopy (RS) analysis can instead be applied directly to cancerous tissues to obtain the corresponding chemical composition, from which

 doi:10.20944/preprints202401.1935.v1

multiple information and pattern scan be extracted and then employed to conduct a precise and fast analysis of the disease. In turn, improvements in the categorization method accuracy can lead to reductions in analysis costs, diagnostic delays, test pervasiveness, and the development of new technologies and software to support an accurate oncology diagnosis. In this sense, RS represents a promising, easy-in-use and low-cost solution to respond to the aforementioned needs. RS is based on the measurement of the so-called Raman effect [2], i. e. a light scattering phenomenon produced by the interaction between the incoming photons and virtual molecular energy levels [3]. The difference between the wavelengths of the scattered and the incident photons is strongly correlated to the chemical properties of the molecular target that determined the scattering. Therefore, by performing a spectral analysis of the radiation scattered by a sample of interest, it is possible to retrieve detailed information about the chemical composition of the irradiated target [4]. Since the Raman effect doesn't involve the interaction between photons and well-defined electronic energy levels, the technique is intrinsically not subject to non-radiative relaxation phenomena, possible source of sample cooling and consequent degradation. This feature makes RS particularly suitable to *in vivo* applications.

Despite the aforementioned strengths, the presence of a large amounts of information characterizing a single Raman spectrum introduces difficulties in the qualitative interpretation of the spectral data. This last issue assumes particular significance in the study of tissues, often characterized by complex chemical composition, alongside with subtle molecular differences between tissues corresponding to different diseases affecting the same organ. For this reason, the application of Machine Learning (ML) techniques could represent a valid solution to systematically retrieve useful information from raw Raman data [5,6].

Several works [7–10] showed how RS in combination with ML could allow to detect malignant tissues in timescales of minutes or even seconds, being a potential help for the surgeon in estimating the tumor margins.

Recently, RS has been applied to chondrogenic tumour classification with excellent results [11]. These first results were followed by further studies of the datasets generated with the application of Deep Learning (DL) methods through wavelet transform of Raman spectra, approaching excellent accuracy [12] or topological features of Raman spectra and ML classifiers trained in combination as an automatic classification pipeline in order to select the best-performing pair [13]. Based on the recent findings on the grading of CS malignant degrees by Raman spectroscopy, in this work, we tested the ability of ML and DL models in the attempt of identifying CS and EC, as case study, with the highest possible accuracy, sensitivity and specificity. The main focus was to distinguish CS from EC and to assign a correct grade to CS. This assignation is often complicated by the fact that RS, giving access to the rich chemical information of the tissues, often does not allow for a complete correspondence between the grades observed through the Raman-based spectral dataset and the malignant degrees commonly assigned by the pathologists through histological examination. So that, for example, what for a pathologist, through the traditional diagnostic technique adopted, is assigned as a grade 2, for a Raman analysis can be a grade 2-1/2, an intermediate value between grade 2 and grade 3, containing chemical characteristics commonly assigned to one of the two degrees of malignancy, respectively. Therefore it becomes extremely important to develop a diagnosis based on Raman spectroscopy alone to have algorithms capable of carrying out this comparison unequivocally and with large accuracy. In this work, we demonstrated which ML models can be adopted for the identification of CS malignant degrees from benign version, EC, on the dataset generated in [11]. In particular, we evidenced the best performances of two models belonging to ML proper and two model belonging to the sub-field of ML called DL. Our criterion to define the best performances of ML-DL models was based on a double requirement: i) to discriminate between CS malignant degrees and EC with high classification accuracy; ii) to retrieve information about the biochemical aspect of the tissues studied, evidenced possible biomarkers.

 doi:10.20944/preprints202401.1935.v1

2. Materials and Methods

2.1. Samples

The study involved ten patients, treated in 2018 in the Azienda Ospedaliero Universiteria Pisana, Pisa, Italy. Among the examined patients, three of which corresponded to the diagnosis of EC, three to CS of grade 1 (G1), two to CS of grade 2 (G2) and two to CS of grade 3 (G3). The resulting bone excised tissues were subjected to formalin-fixing and paraffin-embedding, without decalcification. For each patient, two tissue sections of thickness 5-μm were obtained from the resulting excised masses. After being deposited on a glass slide, commonly employed in microscopy, the paraffin was removed. One of the aforementioned section was stained with Hematoxylin and Eosin for the following histopatological examination. The other one was not subjected to staining and employed for the acquisition of Raman spectra.

2.2. Raman apparatus

The Raman microscope was a Thermo Fisher Scientific DXR2xi Confocal Raman Microscope [14]. The setup collected the Raman back-scattered photons, generated by illuminating the sample with a 532 nm laser emitting at powers between 5 and 10 mW [11]. The optics was composed of a 100$\times$ objective and a pinhole of diameter 25 μm. The resulting Raman spectra were acquired in the range between 400 and 1800 cm^{-1}, with $N_p = 1738$ points for each spectrum.
The final dataset included $N_s = 337$ spectra, 80 spectra for EC, 80 for G1, 84 for G2 and 93 for G3. Finally, the minimum Raman intensity was subtracted from each raw spectrum.

3. Data analysis

In the following, we will represent the Raman data as couples $\{(x_i, y_i)\}$, $i = 1, ..., N_s$, where $x_i \in \mathbb{R}^{N_p}$ is a vector storing the Raman intensities within a single spectrum, while y_i represents the value of the label associated to the i-th spectrum. The spectrum x_i can be also viewed as the i-th row of a matrix X of size $N_s \times N_p$.
As stated in the Introduction section, the main objective of this work was to employ RS in combination with ML to classify bone tissue. In particular, we focused our attention in three distinct classification problems:

1. The problem of distinguishing EC and CS (EC-CS);
2. The problem of distinguishing G1, G2 and G3 (G1-G2-G3);
3. The problem of distinguishing EC, G1, G2 and G3 (EC-G1-G2-G3).

To this aim, we employed three ML protocols:

- *Random Forest Classifier (RFC)*: this non-linear ML algorithm is based on building decision trees by training them on datasets obtained by randomly selecting spectra from the initial dataset. This selection allows the presence of duplicates. The result of this procedure is a "forest", whose prediction is based on the majority of the responses of the trees belonging to it. In this work, we adopted a forest of 4000 trees, to minimize the so-called out-of-bag error [15];
- *Multi-Layer Perceptron (MLPC)*: in this work, this simple DL algorithm consisted in 900 hidden layers and a ReLU activation function. We carried out the training either with the ADAM [16] or with the L-BFGS-B [17] solvers, with an upper limit of 600 iterations. In the following, we will refer to the aforementioned DL models as MLPC(ADAM) and MLPC(L-BFGS-B), respectively;
- *Support Vector Machine (LSVM)*: this ML algorithm is aimed at determining the so-called *maximum-margin hyperplane*, separating the vectors $\{x_i\}$ corresponding to different values of the label [18]. The general equation of an hyperplane can be written as

$$w^T x - b = 0, \tag{1}$$

 doi:10.20944/preprints202401.1935.v1

where w is a vector normal to the hyperplane and b a real constant. According to the linear version of SVM, the classification is performed by solving the following minimum problem:

$$\min_{w,b} w^T w \tag{2}$$

with the constraint $y_i(w^T x_i + b) \geq 1 \; \forall i = 1, ..., N_s$. Despite non-linear and more advanced versions of this algorithm were introduced, we adopted the original linear version as representative of a linear ML model, with the aim of comparing the resulting performances with the aforementioned non-linear ML routines;

The performances of the ML models mentioned before were assessed through 5-fold Cross Validation, in terms of Sensitivity (S), Specificity (SP) and Accuracy (A). The choice of such parameters was motivated by the wide employment in medicine.

One of the purposes of this work was the search for the molecules relevant for the process of classification, with interesting consequences in the understanding of the biochemical processes behind the occurrence of such diseases. In the framework of ML and DL, this problem is referred to as the assessment of the Feature Importance (FI). In this work, we adopted the so-called Permutation Feature Importance (PFI) [19–21]. Consider a ML or DL model M, previously trained on the dataset represented by the matrix X. Let s be a generic score, assessing the performance of M on a test dataset X'. Suppose to calculate the parameter s_j, representing the aforementioned score, on the dataset X' after a permutation of the elements of the j-th column. The basic idea behind the definition of PFI is that, if $s_j \sim s$, the spectral component corresponding to the j-th column of X' can be considered irrelevant for the classification. The PFI associated to the j-th spectral component is defined as

$$PFI_j = s - \frac{1}{K} \sum_{l}^{K} s_{l,j}. \tag{3}$$

in this definition, X' is subjected to K permutations of the j-th column, and $s_{l,j}$ represents the score obtained at the l-th permutation. By definition, the larger PFI_j, the larger the importance of the j-th spectral component. Despite RFC provides an intrinsic definition of FI, based on the ability of a single feature in increasing the "purity" of the classification domains [22], the use of PFI allowed to compare the FI of different ML models and to reinforce our considerations about the relevant chemical compounds in the biochemical processes at the origin of the diseases under interest. In the following, we calculated PFI associated to the prediction accuracy ($s \equiv A$), on a X' dataset obtained by randomly selecting spectra from X, with a proportion of 20% with respect to the total number of spectra. We chose this proportion in line with the 5-fold cross validation adopted.

4. Results and discussion

It us commonly recognized that the progression of the grade of malignancy of CSs is strongly correlated to several biochemical contents of ExtraCellular Matrix (ECM), such as degradation of collagen, cell proliferation or different biochemical composition of non-collagenous proteins in terms of proteoglycans contents [23]. In addition, CSs are characterized by chondrocyte-derived hyaline-like ECM, which generally surrounds the tumor cells [24], whereas hyaline-like ECM is composed of a woven network of collagen fibres and proteoglycans. Raman analysis already evidenced that one of the biomarkers indicating the modifications and degradation of collagen in cancerous tissues is Proline, one of the three amino acids forming the collagen α-helix [11]. This is nor surprising because proline metabolism plays a fundamental role in a number of regulatory targets in mammalian tissues and is particularly important in cancer [25].

In Figure 1 (a), the averaged spectra associated to CS and EC are shown. The shaded areas represent the related standard deviation. The corresponding peak assignments are reported in Table 1. The general behaviour of the averaged spectra highlights a decrease in the Raman signal of CS with

 doi:10.20944/preprints202401.1935.v1

respect to EC. In particular, we qualitatively observed the largest differences between CS and EC in the Raman intensities in the following spectral bands: the most intense peak ($\sim 1003\,cm^{-1}$) can be attributed to Phenylalanine (Phe). The presence of this molecule is testified also by the peak at $1609\,cm^{-1}$. Phe is a precursor of several amminoacids, such as Tyrosine, represented by the peaks at 815, 172 and $1207\,cm^{-1}$. Tyrosine was previously recognized as an amminoacid regulating the production and activity of osteoclasts [26]. We attributed the two narrow peaks at $\sim 729\,cm^{-1}$ to carbonates that, alongside bioapatites (849, 1035, 1057 and $1098\,cm^{-1}$), represent one of the most abundant inorganic components of the bone tissue. The presence of mineral compounds is also testified by the peak at $604\,cm^{-1}$, attributable to mineral phosphate groups. Other relevant spectral components can be found in the peaks at 830 and $1453\,cm^{-1}$, assigned to collagen and CH_2 wag, respectively.

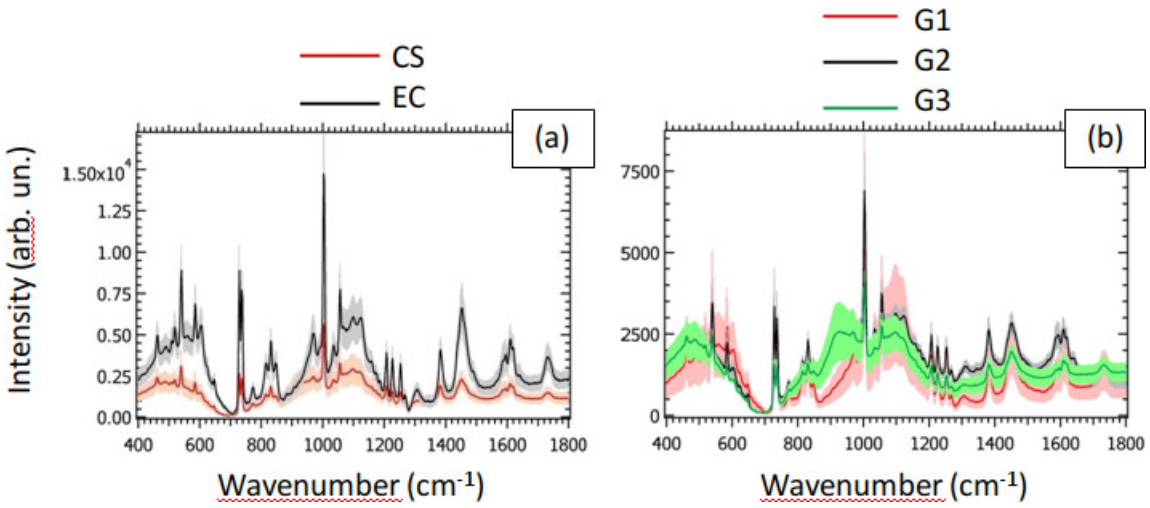

Figure 1. (a) Averaged Raman spectra of CS and EC; (b) averaged spectra of G1, G2 and G3.

The small standard deviations in comparison to the average Raman spectra observed for the CS class in Figure 1 (a) result in small differences between the averaged Raman spectra of G1, G2 and G3, as shown in Figure 1 (b). However, the peak of Phe qualitatively highlights the largest differences between the three grades of CS. This last features makes the peak of Phe a promising candidate for the grading of CS. In Table 2, the performances of the ML and DL models for the examined classification problems are resumed. The Accuracy A, the Sensitivity S and the Specificity SP were averaged over the 5 folds and over the values of the label. The most evident result highlighted is the substantial difference between the performances of the linear SVM with respect to the other models, for all the classification problems considered. This feature reveals how non-linearities in the definition of the models result in enhanced classification performances. As expected, the simplest binary classification problem EC-CS led to the maximum performances, i. e. $A = (99.7 \pm 0.1)\%$, $S = (99.7 \pm 0.1)\%$ and $SP = (99.0 \pm 0.1)\%$, reached with MLPC(ADAM). On the other hand, the classification problem EC-G1-G2-G3 result on the minimum classification accuracies, with the maximum value of $A = (97.6 \pm 0.1)\%$ obtained with MLPC(ADAM). In conclusion, the tested routines showed excellent classification performances, making the technique a promising candidate for future applications in the diagnosis and grading of CS.

In Table 2, the performances of the ML and DL models for the examined classification problems are resumed. The Accuracy A, the Sensitivity S and the Specificity SP were averaged over the 5 folds and over the values of the label. The most evident result highlighted is the substantial difference between the performances of the linear SVM with respect to the other models, for all the classification problems considered. This feature reveals how non-linearities in the definition of the models result in enhanced classification performances. As expected, the simplest binary classification problem EC-CS led to the maximum performances, i. e. $A = (99.7 \pm 0.1)\%$, $S = (99.7 \pm 0.1)\%$ and $SP = (99.0 \pm 0.1)\%$, reached with MLPC(ADAM). On the other hand, the classification problem EC-G1-G2-G3 result on the minimum

 doi:10.20944/preprints202401.1935.v1

classification accuracies, with the maximum value of $A = (97.6 \pm 0.1)\%$ obtained with MLPC(ADAM). In conclusion, the tested routines showed excellent classification performances, making the technique a promising candidate for future applications in the diagnosis and grading of CS.

Table 1. Raman peaks of the analyzed samples within the range between 400 and 1800 cm^{-1} and corresponding peak interpretations [11].

Wavenumber (cm^{-1})	Interpretation	Reference
490	Glycogen	[27]
519	Phosphatidylinositol	[28]
540	Amminoacid cysteine	[28]
584	Phosphate (bend) peak	[29]
604	Phosphate (minerals)	[30]
646	C-P vibrations	[31]
729	Carbonates	[32]
773	Hydroxyapatite	[33]
815	Proline, Hydroxyproline, Tyrosine, ν_2 PO_2^- stretching of nucleic acids	[28]
831	Collagen	[34]
849	Apatite	[35]
971	Tricalcicum phosphate	[36]
1003	Phenylalanine	[37]
1035	Apatite	[38]
1057	$\nu_3 - PO_4^{3-}$ (Apatite)	[39]
1098	$\nu_1 - CO_3^{2-}$ (Hydroxyapatite)	[40]
1123	C-N (Proteins)	[28]
1159	C-C/C-N stretching (Proteins)	[28]
1172	Tyrosine	[41]
1185	Carbohydrates	[42]
1207	Hydroxyproline, tyrosine	[43]
1227	Nucleic acids	[44]
1253	Amide III	[45]
1267	Amide III, lipids	[28]
1307	Amide III, lipids	[46]
1383	N-acetyl-glucosamine	[47]
1453	CH_2 wag	[48]
1489	Guanine	[49]
1595	Amide I	[50]
1609	Amide I, Phenylalanine	[51]
1619	Amide I (aggregates)	[52]
1639	Proteins, collagen	[53]
1731	Ester group	[54]

Table 2. Accuracy A, Sensitivity S and Specificity SP, averaged over the 5 folds and over the values of the label.

Classification problem	Model	$A(\pm 0.1\%)$	$S(\pm 0.1\%)$	$SP(\pm 0.1\%)$
EC-CS	SVM	78.9	78.9	79.7
EC-CS	RFC	98.5	98.5	97.0
EC-CS	MLPC(ADAM)	99.7	99.7	99.0
EC-CS	MLPC(L-BFSG-B)	99.1	99.1	97.1
G1-G2-G3	SVM	75.9	75.9	87.4
G1-G2-G3	RFC	99.2	99.2	99.6
G1-G2-G3	MLPC(ADAM)	99.2	99.2	96.6
G1-G2-G3	MLPC(L-BFSG-B)	99.2	99.2	99.6
EC-G1-G2-G3	SVM	76.6	76.6	92.4
EC-G1-G2-G3	RFC	97.3	97.3	99.1
EC-G1-G2-G3	MLPC(ADAM)	97.6	97.6	99.2
EC-G1-G2-G3	MLPC(L-BFSG-B)	97.3	97.3	99.1

 doi:10.20944/preprints202401.1935.v1

Analogously, Figure 2 reports the PFI associated to the prediction accuracy for the models examined as a function of wavenumbers, for all the classification problems of interest, and where the PFI is normalized with the MinMax rule [55]. We emphasize that the PFI provides a measure of the relevance of a spectral component in the detecting the values of the label. In this sense, the behaviour of PFI for MLPC (Figure 2 (a), (c) and (e)), characterized by the the presence of a large number of peaks of similar intensities, indicates that the DL models studied rely on a large number of spectral components to reach the aforementioned performances. This trend is probably the result of the strong non-linear nature of MLPC. On the other hand, the PFI of SVM and RFC, represented in Figure 2 (b), (d) and (f), show a small number of well-definite peaks in comparison to MLPC. Therefore, despite SVM and RFC showed worse classification performances than the DL models, they are potentially capable of providing more information about the biochemical mechanisms on the basis of the malignant degree under interest. In particular, by observing the Figure 2 (b), we detected a peak of PFI at ~ 602 cm^{-1}, exhibiting large feature importance either for SVM or for RFC. As shown in Table 1, this peak is attributable to phosphate groups associated to mineral compounds, for example hydroxyapatite, as was to be expected. We noted the same feature for the peaks at ~ 730 and ~ 1449 cm^{-1}, corresponding to carbonates and CH_2 wag. These finding, especially the first two wavenumbers mentioned, suggest differences in EC and CS attributable to the mineral components. Analogously, the peak of Phe (~ 1003cm^{-1}) observed either for SVM or for RFC in Figure 2 (d) suggests relevant differences between different grades of CS in the content of this molecule. Finally, as expected, in the classification problem EC-G1-G2-G3, the behaviour of the PFI (Figure 2 (f)) appears to be intermediate between the PFI in the EC-CS and the G1-G2-G3 classification problems.

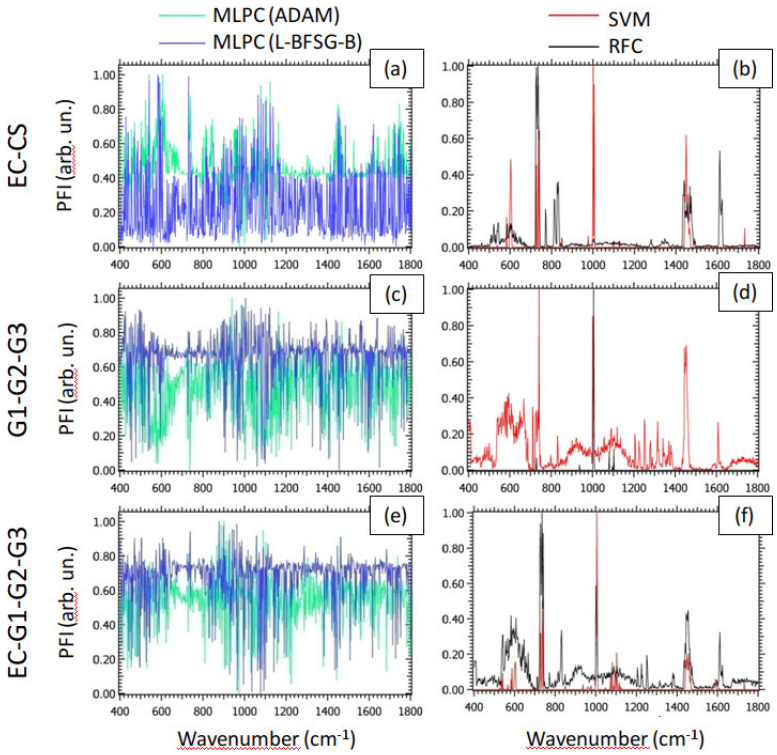

Figure 2. (a) PFI for MLPC(ADAM) and MLPC(L-BFSG-B) in the classification problem EC-CS; (b) PFI for SVM and RFC in the classification problem EC-CS; (c) PFI for MLPC(ADAM) and MLPC(L-BFSG-B) in the classification problem G1-G2-G3; (d) PFI for SVM and RFC in the classification problem G1-G2-G3; (e) PFI for MLPC(ADAM) and MLPC(L-BFSG-B) in the classification problem EC-G1-G2-G3; (f) PFI for SVM and RFC in the classification problem EC-G1-G2-G3. The PFI signals are normalized with the MinMax rule.

 doi:10.20944/preprints202401.1935.v1

5. Conclusions and Future Perspectives

Based on the recent findings based on the application of methods of ML and DL to the grading of CS malignant degrees by Raman spectroscopy, in this work, we tested the ability of different ML and DL models in the attempt of identifying CS and EC, as case study, with the highest possible accuracy, sensitivity and specificity, quickly and at the lowest possible computational costs. The main focus was so to support computationally and in autonomous way (independent by the operator) the distinction between CS from EC and, in the same time, to assign a correct degree to CS tissues.

Paradoxically, this assignation is often complicated by the fact that RS, giving access to the rich chemical information of the tissues, often does not allow for a complete correspondence between the grades observed through the Raman-based spectral dataset and the malignant degrees commonly assigned by the pathologists through histological examination. In addition to this limitation, the ML and DL methods selected by the highest accuracy performances could they could be of considerable help in solving another limitation of RS spectral imaging, namely the intrinsic low acquisition speed. In order to become a standard for pathologists involved in the classification of tumor tissues for a correct and rapid diagnosis, RS must overcome these two limitations. While to overcome the low acquisition speed it will be necessary to adopt improved solutions at instrumental set up, for the interpretation of the Raman spectral dataset of oncological tissues, the possibilities offered by ML and DL methods are crucial. To this aim, we assessed the performances either of selected ML or of DL models. The work resulted in excellent classification performances, especially for the DL models, i.e. MLPC(ADAM) and MLPC(L-BFSG-B), with prediction accuracies approaching 100%. These findings make such models good candidates for future applications in the automated diagnosis and/or in the *in vivo* intraoperative detection of such bone tumors. However, with respect to DL, the use of ML provided precious information about the chemical compounds relevant for the classification, with potential implications in the understanding of the biochemical mechanisms behind the occurrence of such diseases.

Author Contributions: Conceptualization, G.L. and M.D.; methodology, G.L.; software, G.L.; validation, G.L. and M.D.; experimental investigation, M.D.; resources, M.D.; data curation, M.D.; writing—original draft preparation, G.L.; writing—review and editing, G.L.; supervision, M.D.; project administration, M.D.; funding acquisition, M.D. All authors have read and agreed to the published version of the manuscript.

Funding: This research was funded by the Regione Toscana through the TELEMO Project under 146 Grant Ricerca Salute 2018.

Institutional Review Board Statement: The study was approved by the local Ethical Committee Comitato Etico Regionale per la Sperimentazione Clinica della Regione Toscana, Sezione AREA VASTA NORD OVEST (protocol number 14249). An informed consent was collected from all patients. For study participation of patients under the age of 18 years, a specific informed consent from a parent has been acquired (mod. C2; protocol number 14249). All the experiments were carried out in accordance with Good Clinical Practice (GCP) and with the ethical principles of the Declaration of Helsinki.

Informed Consent Statement: Ten patients affected by primary chondrogenic tumors of the skeleton were enrolled in this study. All patients were diagnosed and treated at our Institution, Azienda Ospedaliera Universitaria Pisana, Pisa, in 2018.

Data Availability Statement: The request for data sets, both raw and processed data, generated during the present study can be agreed and made directly to the corresponding author.

Acknowledgments: The authors wish to thank Dr. R. Gaeta and Prof. A. Franchi, from Azienda Ospedaliera Universitaria Pisana, for useful support. The NanoBioTLab CNR-IBF is warmly acknowledged.

Conflicts of Interest: The authors declare no conflict of interest.

 doi:10.20944/preprints202401.1935.v1

Abbreviations and symbols

The following abbreviations are used in this manuscript:

Abbreviation/Symbol	Definition
CS	Chondrosarcoma
EC	Enchondroma
MRI	Magnetic Resonance Imaging
CT	Computed Tomography
RS	Raman Spectroscopy
ML	Machine Learning
CRM	Confocal Raman Microscopy
DL	Deep Learning
ECM	ExtraCellular Matrix
G1	Chondrosarcoma (grade 1)
G2	Chondrosarcoma (grade 2)
G3	Chondrosarcoma (grade 3)
x_i	i-th Raman spectrum
y_i	Value of the label y for the i-th Raman spectrum
X	Training dataset matrix
X'	Test dataset matrix
N_s	Number of Raman spectra
N_p	Number of points of a single Raman spectrum
EC-CS	Classification problem (values of the label: EC and CS)
G1-G2-G3	Classification problem (values of the label: G1, G2 and G3)
EC-G1-G2-G3	Classification problem (values of the label: EC, G1, G2 and G3)
SVM	ar Support Vector Machine
RFC	Random Forest Classifier
MLPC(ADAM)	Multi-Layer Perceptron (ADAM solver)
MLPC(L-BFSG-B)	Multi-Layer Perceptron (L-BFSG-B solver)
FI	Feature Importance
PFI	Permutation Feature Importance

References

1. Weinschenk, R.C.; Wang, W.L.; Lewis, V.O. Chondrosarcoma. *JAAOS-Journal of the American Academy of Orthopaedic Surgeons* **2021**, *29*, 553–562.
2. Raman, C.V.; Krishnan, K.S. A new type of secondary radiation. *Nature* **1928**, *121*, 501–502.
3. Cialla-May, D.; Schmitt, M.; Popp, J. Theoretical principles of Raman spectroscopy. *Physical Sciences Reviews* **2019**, *4*, 20170040.
4. Jones, R.R.; Hooper, D.C.; Zhang, L.; Wolverson, D.; Valev, V.K. Raman techniques: fundamentals and frontiers. *Nanoscale research letters* **2019**, *14*, 1–34.
5. Blake, N.; Gaifulina, R.; Griffin, L.D.; Bell, I.M.; Thomas, G.T. Machine Learning of Raman Spectroscopy Data for Classifying Cancers: A Review of the Recent Literature. *Diagnostics* **2022**, *12*.
6. Lazzini, G.; D'Acunto, M. Grading of Melanoma Tissues by Raman MicroSpectroscopy. *Engineering Proceedings* **2023**, *51*, 10.
7. Jabarkheel, R.; Ho, C.S.; Rodrigues, A.J.; Jin, M.C.; Parker, J.J.; Mensah-Brown, K.; Yecies, D.; Grant, G.A. Rapid intraoperative diagnosis of pediatric brain tumors using Raman spectroscopy: A machine learning approach. *Neuro-Oncology Advances* **2022**, *4*, vdac118.
8. Jelke, F.; Mirizzi, G.; Borgmann, F.K.; Husch, A.; Slimani, R.; Klamminger, G.G.; Klein, K.; Mombaerts, L.; Gérardy, J.J.; Mittelbronn, M.; others. Intraoperative discrimination of native meningioma and dura mater by Raman spectroscopy. *Scientific Reports* **2021**, *11*, 23583.
9. Riva, M.; Sciortino, T.; Secoli, R.; D'Amico, E.; Moccia, S.; Fernandes, B.; Conti Nibali, M.; Gay, L.; Rossi, M.; De Momi, E.; others. Glioma biopsies classification using Raman spectroscopy and machine learning models on fresh tissue samples. *Cancers* **2021**, *13*, 1073.
10. Li, Z.; Li, Z.; Chen, Q.; Zhang, J.; Dunham, M.E.; McWhorter, A.J.; Feng, J.M.; Li, Y.; Yao, S.; Xu, J. Machine-learning-assisted spontaneous Raman spectroscopy classification and feature extraction for the diagnosis of human laryngeal cancer. *Computers in biology and medicine* **2022**, *146*, 105617.

11. D'Acunto, M.; Gaeta, R.; Capanna, R.; Franchi, A. Contribution of Raman spectroscopy to diagnosis and grading of chondrogenic tumors. *Scientific Reports* **2020**, *10*.
12. Manganelli Conforti, P.; D'Acunto, M.; Russo, P. Deep Learning for Chondrogenic Tumor Classification through Wavelet Transform of Raman Spectra. *Sensors* **2022**, *22*. doi:10.3390/s22197492.
13. Conti, F.; D'Acunto, M.; Caudai, C.; Colantonio, S.; Gaeta, R.; Moroni, D.; Pascali, M.A. Raman spectroscopy and topological machine learning for cancer grading. *Scientific Reports* **2023**, *13*. doi:10.1038/s41598-023-34457-5.
14. Rzhevskii, A. The recent advances in Raman microscopy and imaging techniques for biosensors. *Biosensors* **2019**, *9*, 25.
15. Fawagreh, K.; Gaber, M.M.; Elyan, E. Random forests: from early developments to recent advancements. *Systems Science & Control Engineering: An Open Access Journal* **2014**, *2*, 602–609.
16. Kingma, D.P.; Ba, J. Adam: A method for stochastic optimization. *arXiv preprint arXiv:1412.6980* **2014**.
17. Zhu, C.; Byrd, R.H.; Lu, P.; Nocedal, J. Algorithm 778: L-BFGS-B: Fortran subroutines for large-scale bound-constrained optimization. *ACM Transactions on mathematical software (TOMS)* **1997**, *23*, 550–560.
18. Kecman, V. Support vector machines–an introduction. In *Support vector machines: theory and applications*; Springer, 2005; pp. 1–47.
19. Altmann, A.; Toloşi, L.; Sander, O.; Lengauer, T. Permutation importance: a corrected feature importance measure. *Bioinformatics* **2010**, *26*, 1340–1347.
20. Demšar, J.; Curk, T.; Erjavec, A.; Gorup, Č.; Hočevar, T.; Milutinovič, M.; Možina, M.; Polajnar, M.; Toplak, M.; Starič, A.; others. Orange: data mining toolbox in Python. *the Journal of machine Learning research* **2013**, *14*, 2349–2353.
21. Pedregosa, F.; Varoquaux, G.; Gramfort, A.; Michel, V.; Thirion, B.; Grisel, O.; Blondel, M.; Prettenhofer, P.; Weiss, R.; Dubourg, V.; others. Scikit-learn: Machine learning in Python. *the Journal of machine Learning research* **2011**, *12*, 2825–2830.
22. James, G.; Witten, D.; Hastie, T.; Tibshirani, R.; others. *An introduction to statistical learning*; Vol. 112, Springer, 2013.
23. Fletcher, C.; Bridge, J.; Hogedoorn, P.; Mertens, F. WHO Classification of Tumours of Soft Tissues and Bone **2013**.
24. Brown, H.K.; Schiavone, K.; Gouin, F.; Heymann, m.F.; Heymann, D. Biology of Bone Sarcomas and New Therapeutic Developments. *Calcif. Tissue Int.* **2018**, *102*, 174–195. doi:10.1007/s00223-017-0372-2.
25. Phang, J.M.; Liu, W.; Hancock, C.N.; Fisher, J.W. Proline metabolism and cancer: emerging links to glutamine and collagen. *Curr Opin Clin Nutr Metab Care* **2014**, *18*, 71–77. doi:10.1097/MCO.0000000000000121.
26. Shalev, M.; Elson, A. The roles of protein tyrosine phosphatases in bone-resorbing osteoclasts. *Biochimica Et Biophysica Acta (BBA)-Molecular Cell Research* **2019**, *1866*, 114–123.
27. Pathmanapan, S.; Poon, R.; De Renshaw, T.B.; Nadesan, P.; Nakagawa, M.; Seesankar, G.A.; Loe, A.K.H.; Zhang, H.H.; Guinovart, J.J.; Duran, J.; others. Mutant IDH regulates glycogen metabolism from early cartilage development to malignant chondrosarcoma formation. *Cell Reports* **2023**, *42*.
28. Movasaghi, Z.; Rehman, S.; Rehman, I.U. Raman spectroscopy of biological tissues. *Applied Spectroscopy Reviews* **2007**, *42*, 493–541.
29. Rehman, I.; Smith, R.; Hench, L.; Bonfield, W. FT-Raman spectroscopic analysis of natural bones and their comparison with bioactive glasses and hydroxyapatite. In *Bioceramics*; Elsevier, 1994; pp. 79–84.
30. Buchwald, T.; Niciejewski, K.; Kozielski, M.; Szybowicz, M.; Siatkowski, M.; Krauss, H. Identifying compositional and structural changes in spongy and subchondral bone from the hip joints of patients with osteoarthritis using Raman spectroscopy. *Journal of biomedical optics* **2012**, *17*, 017007–017007.
31. Errassifi, F.; Sarda, S.; Barroug, A.; Legrouri, A.; Sfihi, H.; Rey, C. Infrared, Raman and NMR investigations of risedronate adsorption on nanocrystalline apatites. *Journal of colloid and interface science* **2014**, *420*, 101–111.
32. Gunasekaran, S.; Anbalagan, G.; Pandi, S. Raman and infrared spectra of carbonates of calcite structure. *Journal of Raman Spectroscopy: An International Journal for Original Work in all Aspects of Raman Spectroscopy, Including Higher Order Processes, and also Brillouin and Rayleigh Scattering* **2006**, *37*, 892–899.
33. Dippel, B.; Mueller, R.T.; Pingsmann, A.; Schrader, B. Composition, constitution, and interaction of bone with hydroxyapatite coatings determined by FT Raman microscopy. *Biospectroscopy* **1998**, *4*, 403–412.

34. Gaifulina, R.; Nunn, A.D.; Draper, E.R.; Strachan, R.K.; Blake, N.; Firth, S.; Thomas, G.M.; McMillan, P.F.; Dudhia, J. Intra-operative Raman spectroscopy and ex vivo Raman mapping for assessment of cartilage degradation. *Clinical Spectroscopy* **2021**, *3*, 100012.
35. Freeman, J.; Wopenka, B.; Silva, M.; Pasteris, J. Raman spectroscopic detection of changes in bioapatite in mouse femora as a function of age and in vitro fluoride treatment. *Calcified tissue international* **2001**, *68*.
36. Khan, A.F.; Awais, M.; Khan, A.S.; Tabassum, S.; Chaudhry, A.A.; Rehman, I.U. Raman spectroscopy of natural bone and synthetic apatites. *Applied spectroscopy reviews* **2013**, *48*, 329–355.
37. Mandair, G.S.; Morris, M.D. Contributions of Raman spectroscopy to the understanding of bone strength. *BoneKEy reports* **2015**, *4*.
38. Kozielski, M.; Buchwald, T.; Szybowicz, M.; Błaszczak, Z.; Piotrowski, A.; Ciesielczyk, B. Determination of composition and structure of spongy bone tissue in human head of femur by Raman spectral mapping. *Journal of Materials Science: Materials in Medicine* **2011**, *22*, 1653–1661.
39. Mangialardo, S.; Cottignoli, V.; Cavarretta, E.; Salvador, L.; Postorino, P.; Maras, A. Pathological biominerals: Raman and infrared studies of bioapatite deposits in human heart valves. *Applied Spectroscopy* **2012**, *66*, 1121–1127.
40. Timchenko, E.; Zherdeva, L.; Timchenko, P.; Volova, L.; Ponomareva, U. Detailed analysis of the structural changes of bone matrix during the demineralization process using Raman spectroscopy. *Physics Procedia* **2015**, *73*, 221–227.
41. Li, J.; Li, J.; Wang, H.; Chen, Y.; Qin, J.; Zeng, H.; Wang, K.; Wang, S. Microscopic Raman illustrating antitumor enhancement effects by the combination drugs of γ-secretase inhibitor and cisplatin on osteosarcoma cells. *Journal of Biophotonics* **2022**, *15*, e202200189.
42. Woess, C.; Unterberger, S.H.; Roider, C.; Ritsch-Marte, M.; Pemberger, N.; Cemper-Kiesslich, J.; Hatzer-Grubwieser, P.; Parson, W.; Pallua, J.D. Assessing various Infrared (IR) microscopic imaging techniques for post-mortem interval evaluation of human skeletal remains. *PLoS One* **2017**, *12*, e0174552.
43. Lau, C.P.; Ma, W.; Law, K.Y.; Lacambra, M.D.; Wong, K.C.; Lee, C.W.; Lee, O.K.; Dou, Q.; Kumta, S.M. Development of deep learning algorithms to discriminate giant cell tumors of bone from adjacent normal tissues by confocal Raman spectroscopy. *Analyst* **2022**, *147*, 1425–1439.
44. Bautista-González, S.; González, N.J.C.; Campos-Ordoñez, T.; Elías, M.A.A.; Pedroza-Montero, M.R.; Beas-Zárate, C.; Gudiño-Cabrera, G. Raman spectroscopy to assess the differentiation of bone marrow mesenchymal stem cells into a glial phenotype. *Regenerative Therapy* **2023**, *24*, 528–535.
45. Wang, S.; Liang, Z.; Gong, Y.; Yin, Y.; Wang, K.; He, Q.; Wang, Z.; Bai, J. Confocal raman microspectral imaging of ex vivo human spinal cord tissue. *Journal of Photochemistry and Photobiology B: Biology* **2016**, *163*, 177–184.
46. Pavlou, E.; Zhang, X.; Wang, J.; Kourkoumelis, N. Raman spectroscopy for the assessment of osteoarthritis. *Annals of Joint* **2018**, *3*.
47. Gamsjaeger, S.; Klaushofer, K.; Paschalis, E.P. Raman analysis of proteoglycans simultaneously in bone and cartilage. *Journal of Raman Spectroscopy* **2014**, *45*, 794–800.
48. Souza, R.A.d.; Jerônimo, D.P.; Gouvêa, H.A.; Xavier, M.; Souza, M.T.d.; Miranda, H.; Tosato, M.G.; Martin, A.A.; Ribeiro, W. Fourier-transform Raman spectroscopy study of the ovariectomized rat model of osteoporosis. *The Open Bone Journal* **2010**, *2*.
49. Olsztynska-Janus, S.; Gasior-Glogowska, M.; Szymborska-Malek, K.; Komorowska, M.; Witkiewicz, W.; Pezowicz, C.; Szotek, S.; Kobielarz, M. Spectroscopic techniques in the study of human tissues and their components. Part II: Raman spectroscopy. *Acta Bioeng. Biomech* **2012**, *14*, 121–133.
50. Gautam, R.; Ahmed, R.; Haugen, E.; Unal, M.; Fitzgerald, S.; Uppuganti, S.; Mahadevan-Jansen, A.; Nyman, J.S. Assessment of spatially offset Raman spectroscopy to detect differences in bone matrix quality. *Spectrochimica Acta Part A: Molecular and Biomolecular Spectroscopy* **2023**, *303*, 123240.
51. Ciubuc, J.D.; Manciu, M.; Maran, A.; Yaszemski, M.J.; Sundin, E.M.; Bennet, K.E.; Manciu, F.S. Raman spectroscopic and microscopic analysis for monitoring renal osteodystrophy signatures. *Biosensors* **2018**, *8*, 38.
52. Cavalu, S.; Pînzaru, S.C.; Peica, N.; Damian, G.; Kiefer, W. Adsorption behavior of hyaluronidase onto silver nanoparticles and PMMA bone substitute. *Journal Of Optoelectronics And Advanced Materials* **2007**, *9*, 686.

 doi:10.20944/preprints202401.1935.v1

53. Castorina, F.; Masi, U.; Giorgini, E.; Mori, L.; Tafuri, M.A.; Notarstefano, V. Evidence for Mild Diagenesis in Archaeological Human Bones from the Fewet Necropolis (SW Libya): New Insights and Implications from ATR–FTIR Spectroscopy. *Applied Sciences* **2023**, *13*, 687.
54. Hędzelek, W.; Marcinkowska, A.; Domka, L.; Wachowiak, R. Infrared spectroscopic identification of chosen dental materials and natural teeth. *Acta Physica Polonica A* **2008**, *114*, 471–484.
55. Gautam, R.; Vanga, S.; Ariese, F.; Umapathy, S. Review of multidimensional data processing approaches for Raman and infrared spectroscopy. *EPJ Techniques and Instrumentation* **2015**, *2*, 1–38.